Journal of Applied Physics

Elastoplastic and polymorphic transformations of iron at ultra-high strain rates in laser-driven shock waves

Cite as: J. Appl. Phys. **130**, 245902 (2021); https://doi.org/10.1063/5.0076869
Submitted: 28 October 2021 • Accepted: 01 December 2021 • Published Online: 22 December 2021

Semen Murzov, Sergey Ashitkov, Evgenia Struleva, et al.

AIP Publishing

Journal of Applied Physics ARTICLE scitation.org/journal/jap

Elastoplastic and polymorphic transformations of iron at ultra-high strain rates in laser-driven shock waves

Cite as: J. Appl. Phys. **130**, 245902 (2021); doi: 10.1063/5.0076869
Submitted: 28 October 2021 · Accepted: 1 December 2021 ·
Published Online: 22 December 2021

Semen Murzov,[1,2,3,a)] Sergey Ashitkov,[1] Evgenia Struleva,[1] Pavel Komarov,[1] Vasily Zhakhovsky,[1,2,3] Victor Khokhlov,[3] and Nail Inogamov[1,2,3]

AFFILIATIONS

[1]Joint Institute for High Temperatures, RAS, 13/2 Izhorskaya St., 125412 Moscow, Russia
[2]Dukhov Research Institute of Automatics, 22 Sushchevskaya St., 127055 Moscow, Russia
[3]L.D. Landau Institute for Theoretical Physics, RAS, 1A Ak. Semenova av, 142432 Chernogolovka, Russia

Note: This paper is part of the Special Topic on Shock Behavior of Materials.
[a)]**Author to whom correspondence should be addressed:** murzovs@gmail.com

ABSTRACT

Elastoplastic and polymorphic α–ε transformations in iron films induced by ultra-short laser-driven shock waves are studied. Interpretation of time-resolved interferometric measurements is performed using an inverse analysis technique of experimental rear-side velocity profiles. The lasts are obtained by numerical differentiation of free surface displacements detected by probe laser pulses. The inverse analysis techniques are validated in consistent two-temperature hydrodynamics and molecular dynamics simulations of laser energy deposition and diffusion, generation, and propagation of shock waves in a polycrystalline iron sample. The stress–strain diagrams containing information about elastoplastic deformation and phase transformation are reconstructed by the inverse analysis. We found that the polymorphic transformation in iron under picosecond duration of loading requires much higher stress in contrast to that in microsecond-scale plate-impact experiments. Moreover, such transition may be accomplished partially even at very high stresses if an unloading tail after the shock front is too short.

I. INTRODUCTION

High-energy nanosecond laser pulses are widely used for studying shock-loaded materials, in particular, to determine the equations of state in extreme conditions.[1,2] However, mechanical response of the material is determined not only by the magnitude of pressure but also by the applied strain rate. Extreme strain rates can be achieved in ultra-short shock waves (SW) generated by femtosecond laser pulses with intensities enough to generate pressures of tens of GPa in solids.

Last two decades, the kinetics of elastoplastic and polymorphic transformations induced by such ultra-short SW in solids came to the attention.[3–22] Various experimental and theoretical research studies show very steep growth of stress barriers for shock-induced elastoplastic transformation and polymorphic transition in metals.[10–17] It has been theoretically proven[7–9] that a high-pressure ultra-short shock may propagate as an elastic shock wave with a speed higher than a speed of a normal elastic precursor wave. Such high-speed shock waves were detected a decade before in experiments with femtosecond laser shock generation.[3–6]

The several models were developed in order to analyze the metal response to ultrashort laser heating;[7,23–26] however, the laser SW in iron has a more complex wave structure than in simple metals without solid–solid phase transition.

Typically, the laser pulse energy is absorbed by an electron subsystem of metal within a thin skin layer. Then this energy diffuses in the depth and heats the ion/lattice subsystem. Thus, the heated layer with high thermal pressure is formed during several picoseconds after a pulse. Thermal expansion of the heated layer generates two opposite compression waves in the glass substrate and the metal.[24,27–29] These waves propagates into the bulk, while thermal energy remains almost in the heated layer. A compression wave is followed by an unloading tail, which results in very fast loading–unloading of material within tens of picoseconds. Such extreme strain rate of the order of 10^{10} s^{-1} may lead to the non-

typical response of the material in comparison to that observed at micro- and nanosecond compression.

Ultrashort loading for times shorter than 100 ps makes possible to observe the highly non-equilibrium metastable states of solids and study material response at the extremely high strain rates.[2,30] In particular it is feasible to reach an ultimate (theoretical) strength of some metals using picosecond and femtosecond laser pulses.[10–14,19–22,30,31] To record kinematics of a free surface with subnanosecond time resolution, the pump–probe chirped pulse interference method is applied.[11,12,20,32]

The shock Hugoniot of elastic metastable states in 99.9% pure iron is measured for films of 250 and 540 nm thickness.[20] The maximal stress behind a shock front was up to 27 GPa for a 250 nm film. The maximal shear stress of 7.9 GPa is higher than one obtained in DFT calculations,[33,34] which may be interpreted as shear modulus hardening in metastable elastic states.

Polymorphic transformation under microsecond shock loading has been studied in different metals and semiconductors.[35] Since iron and steel are widely used constructive materials, their behavior in extreme conditions is actively studied for the last several decades. There are four polymorphic phases of iron:[36] the body-centered cubic (bcc) α-iron is stable at low pressures and temperatures, γ-iron has a face-centered cubic lattice, δ-iron has a high-temperature bcc lattice, and ε-iron has a hexagonal close-packed (hcp) lattice. The $\alpha \rightarrow \varepsilon$ transformation in iron[37] was observed as a plateau on shock Hugoniot studied experimentally in sub-microsecond shocks.[38–41] The plateau at 13 GPa indicates a density change due to the transformation to high-pressure ε phase. A triple shock wave structure in iron was observed in Refs. 21 and 38–42. The first wave is an elastic precursor associated with the 0.5 GPa yield strength for sub-microsecond loading. The second is a plastic wave in α-iron, and the last density jump is formed due to $\alpha \rightarrow \varepsilon$ polymorphic transformation. Backward transformation in the rarefaction wave (RW) has a lesser than 13 GPa pressure and leads to hysteresis in stress–strain $\sigma - V/V_0$ diagram. As it was found in Refs. 20, 43, and 44, the kinetics of the $\alpha \rightarrow \varepsilon$ transformation in iron depends on the duration of existence in the shock compressed state. The aim of this work is to further study this kinetics.

The polymorphic transformation to ε iron initiated by stress of 25 GPa was observed in Ref. 21, where the free surface velocity of 1.2 and 1.4 μm iron films was measured to calculate the stress–strain $\sigma - V/V_0$ diagram. Such high stress is an approximately two times higher than one required for the transition under microsecond compression. However, a three-wave configuration of shock fronts was not observed because of a low plastic relaxation rate.

Typical duration of shock compression is within a microsecond time range in plate-impact experiments,[45–48] except the 200 ps laser pulse duration employed in Ref. 21. The 1.2 ps pump pulses are used in this work, which is two to three orders of magnitude shorter than in the above experiments. We use a similar configuration of the iron film placed on the transparent glass substrate through that an ultrashort laser pulse reaches the film where it is partially reflected and absorbed in iron. To reconstruct a stress–strain diagram, an inverse analysis technique for the measured rear-side velocity profiles is developed in decades.[45,46] We improve this theoretical approach by including an unloading part of the profile in order to detect the polymorphic transformation not only at a compression part of the pathway in a stress–strain diagram. A piece-wise quasi-stationary approximation is also used in reconstruction, i.e., a shock wave is assumed to be steady during propagation in a film with the minimal thickness of 480 nm in our experiments. Validation of the inverse analysis is based on comparison with results of molecular dynamics simulation of shock compression of polycrystalline iron.

II. MEASUREMENT OF REAR SURFACE POSITION IN IRON FILMS

A. Experimental setup and methods

Time and spatial resolved spectral interferometry[32] was used to investigate material response to laser-induced shock-wave compression in iron films in a picosecond range. The femtosecond Ti: Sapphire laser was a source of pump and probe pulses. A single ultra-short pump pulse was focused on a metal film surface through a glass substrate to generate shock, as illustrated in Fig. 1.

Part of the 300 ps chirped probe pulse with a spectral width of 40 nm at a central wavelength $\lambda_0 = 795$ nm was separated after the amplifier to probe the rear surface of the film.

The pump radiation was focused onto the surface of an iron sample **4**, as shown in Fig. 1, through a transparent substrate by the lens with a focal length of 20 cm. A laser spot with a spatial Gaussian distribution of intensity has a radius $r_0 = 30\,\mu$m at the one sigma level.

Such spot size ensures practically uniaxial compression of the micrometer-thick target material because the spot size is much larger than the iron film thickness. The pulse energy was smoothly varied using a polarization attenuator **3**. After each laser pulse, the sample was moved by about 200 μm to a new location using the *9* micromanipulator.

Heating through the glass substrate limits the peak intensity of pump laser pulse due to the possible occurrence of nonlinear effects and optical breakdown in the glass. To decrease the peak intensity, the heating pulse duration is increased from 40 fs to 1.2 ps by tuning the compressor of the laser system appropriately. In the described experiments, the laser pulse energy was $E = 100 \pm 5\,\mu$J, which corresponds to the incident energy density at the center of the focal spot at $F_0 = 3.4\,\mathrm{J/cm^2}$. The pulse energy in the experiments was specially selected to generate the maximum amplitude compression pulses in the samples. Exceeding the energy E leads to distortion of the recorded rear-side displacements and decrease in the free surface velocity associated with the development of optical breakdown and absorption of radiation in the glass substrate.

To diagnose the dynamics of displacement $z(t)$ of the rear surface of a metal film during the exit of a shock wave, a Michelson interferometer in imaging configuration ***5*** and an Acton-2300i diffraction spectrometer (Czerny-Turner scheme) ***6*** with a diffraction grating of 600 lines/mm were used as shown in Fig. 1. Image transfer was carried out using an objective Olympus with a numerical aperture NA = 0.3, providing a spatial resolution in the target plane of 2 µm. Optical signals at the output of the spectrometer were recorded using a SensiCam QE CCD camera ***7*** with a cooled matrix of 1375 × 1375 px in size and 12-bit wide. The applied optical scheme provides continuous registration of the dynamics of

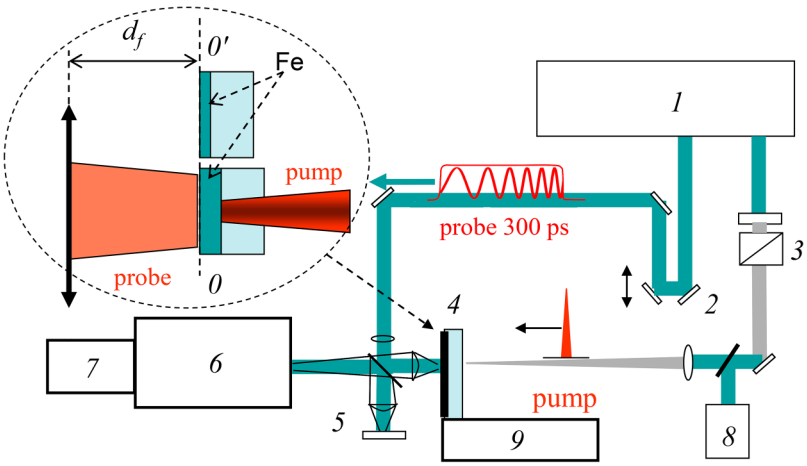

FIG. 1. Experimental scheme: 1—Ti:S laser, 2—optical delay line, 3—polarizing attenuator, 4—sample, 5—Michelson interferometer, 6—diffraction spectrometer, 7—CCD camera, 8—photo detector, and 9—micromanipulator. Circular inset shows the thin and thick iron films at the object plane $0 - 0'$.

the process with a time resolution of $\delta t \approx 1$ ps in the temporal interval $\Delta t = 0$–200 ps.

The experimental samples were Armco iron films with a thickness of 480, 580, 740, 970, and 1160 nm, deposited by the magnetron sputtering on glass substrates with a thickness of 150 μm. An Armco iron plate with a purity of 0.95 was used as a magnetron target. The thicknesses of samples were measured in the area of laser irradiation using the atomic force microscope (Veeco Multimode 5) with an accuracy of ± 5 nm.

In the experiments, the free surface of studied samples with different thicknesses was positioned using a micromanipulator **9** into the object plane $0 - 0'$ of the interferometer objective (see the circular inset in Fig. 1) with an accuracy of no worse than $\delta d_f \approx 2$ μm. The tuning was carried out according to the maximum contrast of the interference fringes. In this case, the accuracy of setting a single (relative) time scale of measurements when changing samples with different film thicknesses is less than 100 fs, which is significantly less than the time resolution of measurements. This error is a sum of differences in the thickness of substrates and the positioning accuracy of the sample surface, which totally does not exceed 10–20 μm. By dividing the thickness error by the speed of light, the indicated uncertainty is less than 100 fs. For the given set of film thicknesses, the difference in times of shock arrival on the rear surface is about tens of picoseconds. Therefore, the measurement error of the difference in the SW emergence times associated with the positioning accuracy and the difference in sample thickness can be neglected.

To determine a zero time, an additional 20 nm thick film was used in our experiment like in.[3] The thickness of this film is comparable to the depth of laser pulse absorption in the iron film. The pulse energy is absorbed by conduction electrons, and then it is transferred to ions during the characteristic time of electron–phonon energy transfer lasting about a few picoseconds,[49] after which the rearside surface of film begins to move. Note that the same processes of laser pulse absorption and heating of iron take place after laser irradiation of a neighbour thick film. Thus, the start of displacement in the film of 20 nm thickness can be taken as an initial time count $t_0 = 0$. This time is associated with the absolute travel time of the compression pulse from the heated subsurface layer to the free rear-side surface for all films. Therefore, the accuracy of determining the arrival is estimated at the level of ± 1 ps.

The Fourier analysis of interferometry data together with the normalizing procedure of phase distributions are used in data processing. This algorithm allows to reconstruct the spatiotemporal phase shift distribution of the reflected probe wave $\Delta\varphi(x, t)$. The magnitude of surface displacement Δz is related to the phase shift by the following relation:

$$\Delta z = \lambda_0 \Delta\varphi / 4\pi. \quad (1)$$

Three interferograms are recorded in each experiment: the interferogram of the sample surface before the exposure (*initial*), at the moment of the SW release (*transient*), and after the end of process—a few seconds after the exposure (*final*). Comparison of the initial and *transient* interferograms provides information on the spatiotemporal dynamics of the SW profile.

Figure 2 shows an example of a space-time distribution of the probe pulse phase $\Delta\varphi(x, t)$ in the $h = 740$ nm film irradiated by an laser pulse with energy $E = 100$ μJ. This distribution describes the dynamics of spatially non-uniform motion of the rear surface at the SW arrival time.

Thus, the measurement scheme provides continuous registration of the surface displacement $\Delta z = \Delta z(t)$ of a sample as a function of time with a spatial resolution $\delta y \approx 2\,\mu$m along the radius in the plane of sample. The time resolution $\delta t = 1$ ps in the range of 0–200 ps is determined by spectrometer dispersion. The algorithm of the Fourier analysis of two-dimensional interferograms[50] with the procedure for normalizing phase distributions provides an error in measuring the phase shift of the probe pulse at the level of $\delta\psi \approx 0.01$ rad, which corresponds to the error in determining the magnitude of surface displacement by level $\delta z \leq 1$–2 nm. The velocity profiles $u_{fs}(t)$ of free surface presented in Fig. 3 for the films under study were obtained by differentiating and smoothing the profiles $\Delta z(t)$ as described in Ref. 20.

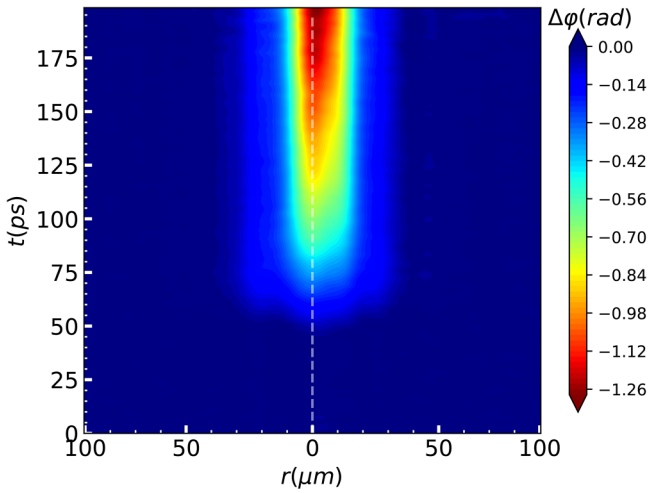

FIG. 2. Spatiotemporal distribution of the probe pulse phase shift before and during rear-surface deformation caused by arrival and reflection of SW in the film of 740 nm thick. The dashed line shows a cross section to construct the displacement profile $z(t)$. The colorbar indicates phases in radians.

III. INVERSE ANALYSIS OF KINEMATIC DATA

A. From kinematics to dynamics and internal states of the environment

There are different methods to analyze shock-wave data. An analytical decomposition of wave profiles onto simple waves is a classical one, which means a manual extraction of information about SW arrival and detection of steep changes in the profiles.

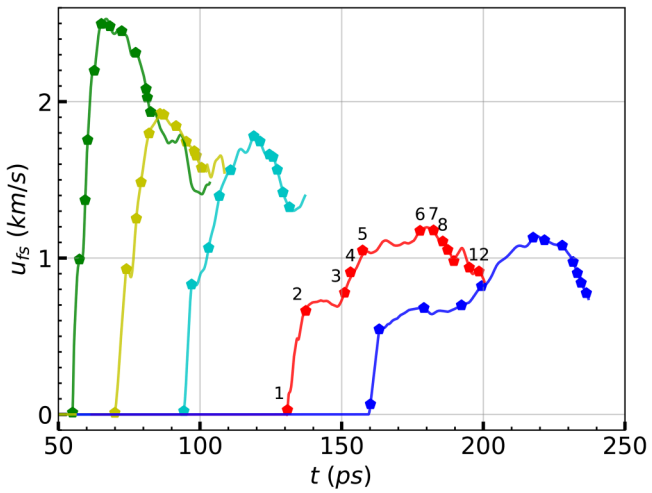

FIG. 3. Free surface velocity profiles for films with thicknesses $h_{1,\ldots,5}$ from left to right: 480, 580, 740, 970, and 1160 nm. The 12 characteristic points are selected on each profile to approximate the experimental dependencies for using the inverse analysis.

The physical effect observed in each profile is then interpreted in terms of model assumptions of elastic–plastic and polymorphic transformations by using the Hugoniot relations with taking into account assumptions on the deviatoric stress, which provides an appropriate strain decomposition onto elastic and plastic parts.[51]

Another theoretical approach is numerical modeling using mechanical or hydrodynamic methods. It can be employed if an analytical approach is difficult to apply for a complex physical model or phenomenon. Usually, a series of simulations is used for tuning parameters of the model matching experimental and simulated profiles. As far as the material model should be usually extended by a simplified phenomenological model that is tuned to minimize residue of simulation and experiment. In a work,[42] a series of numerical simulations at microsecond times under the plane SW in iron is studied to formulate the polymorphic transformation model.

Here the more complex phenomena are observed. The polymorphic transition and elastic–plastic transformation in iron need at least several picoseconds to be completed. The stresses for elastoplastic and phase transformations produced by an ultrashort picosecond SW would be close to the ultimate values at the strain rates higher than $\approx 10^9\ s^{-1}$. Ultrashort effects on the iron are considered in this work using the peculiar material models described below. The material model should describe an absorption of radiation and two-temperature (2T) physics—the electron heat conduction within an electron subsystem and the electron–ion energy exchange. The model should describe the transformation of femtosecond heating into pressure where thermal and dynamic parts of the problem are synthesized. 2T hydrodynamic calculations are discussed comprehensively in Ref. 52. High-temperature thermodynamic states of iron generated by almost isochoric laser heating have tens of gigapascals of thermal pressure. Such a huge pressure accumulated in a thin subsurface layer generates an SW. After leaving the heated layer and the zone of thermal expansion, the SW propagates further in a cold solid phase. This SW propagation toward the rear side of film should be calculated using an elastoplastic model for solid iron taking into account the kinetics for the polymorphic phase transition.

Another approach is proposed here for obtaining density $\rho(h, t)$ and the longitudinal stress $\sigma(h, t)$ avoiding numerical integration of 2T hydrodynamics equations and deformable solid. The function $u_{fs}(h, t)$ is approximated on the basis of experimental results for different film thicknesses h. The approach requires experiments for at least two[21] or three[47] different thicknesses h of the film depending on the order of the approximating polynomials. We use a piecewise linear interpolation of the velocity profiles as a function of two variables; therefore, an approximation of only the first derivative of the free surface velocity is included in the model. Since the initial profiles are coordinates of free surface of different films, the usage of a higher order approximation means an approximation of a third derivative of measured displacement. Knowing the shock Hugoniot of iron, the phase state is determined from values of ρ and σ.

B. Inverse analysis technique

The technique is based on the reconstruction of the free surface velocity $u_{fs}(t, h)$ in two variables—time t and the

Lagrangian coordinate h. Inverse calculation of stress–strain pathways based on the experimentally measured profiles of free surface velocity $u_{fs}(t)$ was first proposed in Ref. 45. Further development of this technique could be found in Refs. 21, 47, and 48.

The first step is approximation of the function $u_{fs}(h, t)$. The approximation relies on reference points corresponding to physically identical kinks on the velocity profiles for different values of h. Each free surface velocity profile is recorded experimentally for a given iron film. This profile can be represented by a precise dependence of velocity $u_{fs}(t)$ on time. For transformation of the free surface velocity to the mass velocity u (the velocity of a selected Lagrangian particle), a relation $u_{fs} = 2u$ is used. The relation is valid in the linear acoustics approximation as long as the pressure is much lower than the bulk modulus, which is 170 GPa for iron. The result is a set of profiles measured with high resolution in time but for several sample thicknesses; as an example for two thicknesses in Ref. 21. In this work, the time-dependent free surface velocities for five different film thicknesses are utilized.

To calculate the longitudinal stress σ and deformation $\mu \equiv 1 - V/V_0$, it is required to integrate the Lagrange equations of motion in certain limited range of experimental data,

$$\frac{\partial \mu}{\partial t} = -\frac{\partial u}{\partial h}, \tag{2}$$

$$\frac{\partial \sigma}{\partial h} = -\rho_0 \frac{\partial u}{\partial t}. \tag{3}$$

To determine the stress at point (t_1, h_1), it is necessary to integrate the Eq. (3) over h from the boundary point h_b,

$$\sigma(t_1, h_1) - \sigma(t_1, h_b) = -\rho_0 \int_{h_b}^{h_1} \frac{\partial u}{\partial t}(h, t_1) dh. \tag{4}$$

To calculate the deformation at point (t_1, h_1), the Eq. (2) is integrated over time t from the boundary point t_b,

$$\mu(t_1, h_1) - \mu(t_b, h_1) = -\int_{t_b}^{t_1} \frac{\partial u}{\partial h}(h_1, t) dt. \tag{5}$$

The boundary functions $t_b(h)$ or its inverse functions $h_b(t)$ define a domain with $\sigma = 0$ and $\mu = 0$, i.e., an iron particle is in a state before the incident SW arrival. The second integration limit in both Eqs. (4) and (5) is selected for interested points on the profile—t_1 or h_1. Setting boundary conditions gives the domain where the function $u(h, t)$ takes nonzero values. Finally, we have a finite time and space domain of experimental profiles for several film thicknesses (here five profiles), but at high time resolution $\Delta t \approx 1$ ps.

C. Kinematic data integration

In order to build up the map of $u(h, t)$, we use the reference points from free surface velocity profiles as illustrated in Fig. 4. The simplified linear form of velocity approximation is utilized here in contrast to a quadratic form,[47]

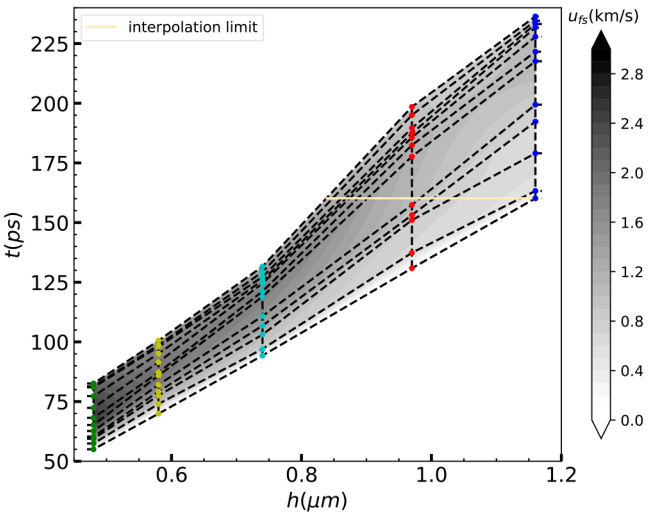

FIG. 4. Map of free surface velocity $u_{fs}(h, t)$ interpolation defined by the doubled velocity from Eq. (6) is shown by shades of gray on the nonuniform mesh of t–h points. Dashed functions $t_i(h)$ are obtained by connecting these points with segments. Positions and colors of the reference points are the same as in Fig. 3.

$$u(h, t) = \frac{u_i(h)(t_{i+1}(h) - t) - u_{i+1}(h)(t - t_i(h))}{t_{i+1}(h) - t_i(h)}, \tag{6}$$

where $t_i(h) < t < t_{i+1}(h)$ is obeyed, and $t_i(h)$ and $u_i(h)$ are functions defined by a piecewise linear interpolation and by a cubic spline, respectively. Subscript i corresponds to the different reference points manually selected on each $u_{fs}(t)$ profile. Moments of time are obligatory chosen with increasing $t_i(h) > t_{i-1}(h)$ with index i. The function $h_i(t)$ denotes an inverse function of $t_i(h)$.

Analysis accuracy is an important characteristic due to the small number of profiles for different h and manual choice of reference points on profiles. It was studied, for example, in Refs. 45 and 47, where it has been indicated that the error of the method reaches a maximum for profiles with the smallest and largest film thicknesses from an available set. Here the partial derivatives in Eqs. (4) and (5) are approximated by the finite differences, and the integration is performed numerically, unlike,[45,47] where the calculation is carried out with an analytical piecewise function $u(h, t)$ which antiderivatives are calculated in advance. For interior points, the central difference is applied,

$$\frac{u(h + \Delta h, t) - u(h - \Delta h, t)}{2\Delta h}.$$

For points near the boundary of the domain of definition, the derivative

$$\frac{\partial u}{\partial h} \approx \Delta u / \Delta h \tag{7}$$

is approximated by a central finite difference, except for the thinnest film where a directed finite difference is used,

$$\frac{u(h_s, t) - u(h_s - \Delta h, t)}{\Delta h},$$

$$\frac{u(h_l + \Delta h, t) - u(h_l, t)}{\Delta h}.$$

Here, h_s and h_l are points on the computational domain boundary. The step $\Delta h = (h_l - h_s)/N$ with $N = 300$ is selected to achieve convergence of integration. One of the features of the method for integrating the system of Eqs. (2) and (3) of kinematic relations, which differs it from the classical approaches (the time of arrival of the wave is recorded, the jump in the mass velocity at a known thickness of the sample), is that the stress–strain diagram depends only on the relative position of the profiles for films of different thicknesses. Thus, a shift in the arrival time of an incident SW in all experiments or a change of all film thicknesses by the same value will preserve the diagram in the mathematical sense. But here, the absolute time is taken into account and the invariance on shift of time or thickness vanishes. For a film with the smallest thickness, it is proposed to use the absolute arrival time of SW and the free surface velocity for the elastic precursor—the point labeled 2 in Fig. 3 on the profile of the corresponding $h = 480$ nm film. The assumption that a wave moves with the constant velocity $U_{s1} = h_1/t_2(h_1)$ is used for this case; therefore, $t_2(h_1)$ is the time corresponding to the point 2 on the profile for the thinnest film of $h_1 = 480$ nm. As a result, it is possible to estimate the derivative

$$\frac{\partial u}{\partial h} \approx \frac{\partial u}{\partial t} U_{s1}^{-1}. \tag{8}$$

Expressions for the partial time derivatives are calculated in a similar way,

$$\frac{\partial u}{\partial t} \approx \Delta u(t)/\Delta t. \tag{9}$$

Time step $\Delta t(h) = (t_l(h) - t_s(h))/N$, where the difference between the first $t_s(h)$ and the last $t_l(h)$ is the set of reference points defined on the $u_{fs}(t)$ profile for a given thickness; therefore, it depends on h.

D. Validation of inverse analysis technique

The initial 2T stage of laser energy absorption and redistribution is simulated by the 2T hydrodynamics method. When exposed to short laser pulses, the temperature of electrons absorbing laser radiation significantly exceeds the temperature of the ion subsystem. 2T hydrodynamics includes the models of processes of electron–ion energy exchange and electron thermal conductivity. At times before the completion of electron–ion relaxation, the electron and ion subsystems have their own quasi-equilibrium temperatures T_e and T_i.[53] At sufficiently high laser pulse energy, the material motion becomes noticeable even in the 2T stage, which makes it necessary to consider thermal diffusion together with material motion within a 2T hydrodynamics approach.[54] The duration of 2T stage, during which $T_e \gg T_i$, is determined by a rate of electron–ion relaxation, which can be long due to the large difference between electron and ion masses. The 2T hydrodynamic equations are listed and discussed in Refs. 55 and Ashitkov:2016:JPCC. This system of equations is closed by equations of state (EoS) for ion and electron subsystems, together with the models of electron thermal conductivity and electron–ion energy exchange. Phonon thermal conductivity is assumed to be negligible compared to electron one.

The tabulated wide-range EOS for the ion subsystem of solid iron in the α-phase (without contributions from the electron subsystem) is given in Refs. 56–58. Analytical formulae for the electron subsystem constructed for various transition metals[59–61] are utilized for iron in our 2T hydrodynamics. Those formulae were fitted to DFT results obtained with the VASP package.

During the laser pulse, the displacement of the material is very small. The thermal source Q describing the absorption of laser radiation in the metal placed at $x^0 > 0$ can be taken in the simplest form with a spatial profile frozen into the substance depending only on the initial position of Lagrangian cells x^0,

$$Q(x^0 > 0, t) = \frac{F_{abs}}{\sqrt{\pi} d_{skin} \tau} \exp\left[-\frac{x^0}{d_{skin}} - \left(\frac{t}{\tau}\right)^2\right]. \tag{10}$$

Here, F_{abs} is an absorbed fluence, d_{skin} is an absorption skin depth, and τ is a pulse duration. The time t is counted from the maximum of laser pulse. We take $F_{abs} = 400\,\mathrm{mJ/cm^2}$, $d_{skin} = 15$ nm, and $\tau = 0.5$ ps for 2T modeling.

There are no free electrons assumed in the glass, instead a one-temperature hydrodynamics with a caloric (Mie–Grüneisen type) equation of state is used. The initial density in glass is $\rho_0 = \rho_{0,\,glass} = 2.2\,\mathrm{g/cm^3}$. Heating of the glass placed at $x^0 < 0$ is described with a heat source as follows:

$$Q(x^0 < 0, t) = \frac{F_{glass}}{\sqrt{\pi} d_{glass} \tau} \exp\left[\frac{x^0}{d_{glass}} - \left(\frac{t}{\tau}\right)^2\right], \tag{11}$$

where $F_{glass} = 700\,\mathrm{mJ/cm^2}$ and $d_{glass} = 50$ nm.

In 2T hydrodynamics simulation, the velocity of the Lagrangian cell with the initial position at 150 nm has been recorded for the usage in MD simulation. Then, the recorded velocity is associated with a piston driving a shock wave in MD simulation. In fact, such a piston transfers smoothly the compression wave from 2T hydrodynamics to MD.

MD simulation provides a complete information about positions and velocities of all atoms at any time, which is used to calculate the stress–strain diagram of shocked iron. We use the $\sigma - V/V_0$ pathways from MD to compare them with stress–strain data calculated with using the only kinematic information about the rear-side surface motion from the same MD simulation.

MD simulation is performed with a sample having dimensions of $600 \times 60 \times 10\,\mathrm{nm^3}$ composed of a small polycrystalline subsample with dimensions $60 \times 60 \times 10\,\mathrm{nm^3}$ repeated by 10 times along the x-axis of wave propagation. The subsample consists of four crystalline grains randomly oriented in the (x, y)-plane, but those grains have the same lattice orientation along the z-axis. Motions

of several Lagrangian particles, which are bunches of atoms targeted within 0.25 nm thick slices at different x-positions, were recorded during MD simulation. The 10 Lagrangian particles with coordinates (the initial position of the particles) are chosen at $h = \{150, 160, 200, 250, 300, 350, 400, 450, 500, 550, 600\}$ nm, see Fig. 5. The approximation of the function $u(h, t)$ is shown in Fig. 6 with the nodal points and shades of gray selected according to the free surface velocity.

Figure 7(a) shows the elastic and plastic shock Hugoniots of α-iron, the shock Hugoniots of real ε-iron and simulated ε-iron with the used MD potential. To check an accuracy of the inverse analysis, several stress–strain states for films of 250 and 500 nm are reconstructed. The obtained points are presented by color symbols in Fig. 7(a). Those points lie on the stress–strain $\sigma - V/V_0$ pathways (solid lines of the same color) gained directly from MD simulation. Thus, the method reconstructs well the stresses and strains gained directly from the MD simulation.

Figure 7(b) shows the stress-time dependencies for several Lagrangian particles. Solid lines correspond to the stress-times gained directly from MD, but symbols indicate data reconstructed by the inverse analysis. The last time moment when the stress history can be inversely obtained is limited by the moment of SW arrival at the Lagrangian particle with the largest initial coordinate. A good agreement between the stress-time profiles supports the validity of the implemented inverse analysis method.

2D maps of the local order parameters of atoms Q_4 and Q_6 as in Steinhart's work[62,63] are shown in Fig. 7(c). The direct and backward phase transformations produced by propagation of an ultrashort shock wave are seen clearly.

To visualize the atomic structure simulated by MD, the central symmetry parameter[64] is routinely used, but it is not enough sensitive to distinguish various crystal lattices. Difficulties are associated with increasing fluctuations of interatomic distances and angles with increasing pressure and temperature. Here, the modified central symmetry parameter C_S is used to reduce the effects of such fluctuations. It is defined for a given k-atom as

$$C_S(k) = \sum_{i<j} \left(1 + [(\vec{r}_{ik} + \vec{r}_{jk})/(c\overline{r_k})]^8\right)^{-1},$$

where i, j-atoms are neighbors of k-atom, $c \approx 0.1 - 0.2$ is the Lindemann constant for melting criterion, and $\overline{r_k}$ is a mean interatomic distance in the neighborhood of k-atom. It provides $C_s = 3$, 6, and 7 for perfect *hcp*, *fcc*, and *bcc* lattices, respectively, but still its accuracy suffers from high temperatures. The advantage of Steinhart's parameters is higher specificity for lattice types and weak temperature dependence at the acceptable computational cost.

The functions Q_{lm}, from which the local order parameters are derived, depending only on the angles between the radius vectors $\vec{r}_{ij} = \vec{r}_j - \vec{r}_i$ from a given i-atom to the neighboring j-atoms, can be calculated as

$$\overline{Q}_{lm}(i) = \langle Y_{lm}(\theta(\vec{r}_{ij}), \phi(\vec{r}_{ij}))\rangle,$$

$$Q_l^2 = \frac{4\pi}{2l+1}\sum_{m=-l}^{l} |\overline{Q}_{lm}|^2,$$

where Y_{lm} are spherical harmonics and θ and ϕ are polar and azimuth angles of the spherical coordinate system for vector $\vec{r}_{ij}$, respectively. Averaging is performed over neighboring atoms chosen with using a Voronoi decomposition around the i-atom position. The local order parameters Q_l are invariant with respect

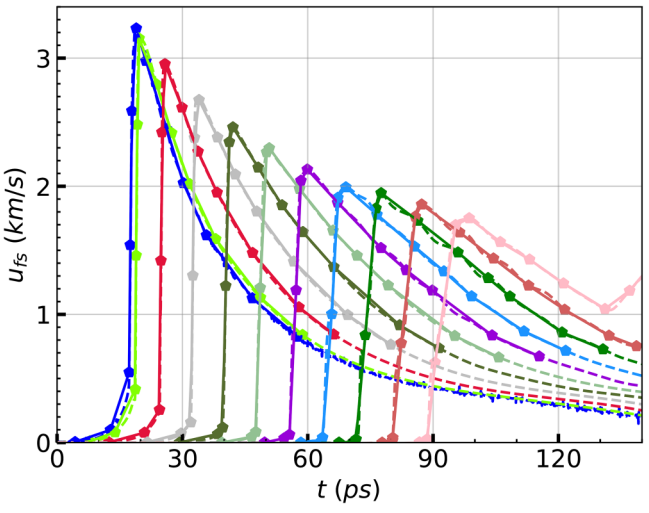

FIG. 5. Doubled velocities of Lagrangian particles at initial positions of 150, 160, 200, ... 600 nm extracted from MD simulation are shown by dashed lines. The reference points of each profile are interpolated by a piecewise linear function drawn with a solid line.

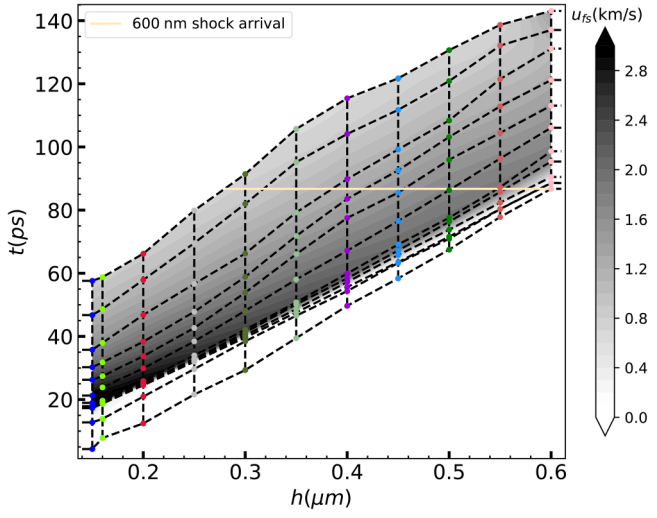

FIG. 6. Interpolation map of doubled velocities of Lagrangian particles $u_{fs}(h, t)$ is shown by shades of gray on the non-uniform mesh of t–h points. Dashed functions $t_i(h)$ are obtained by connecting these points with segments. Positions and colors of the reference points are the same as in Fig. 5.

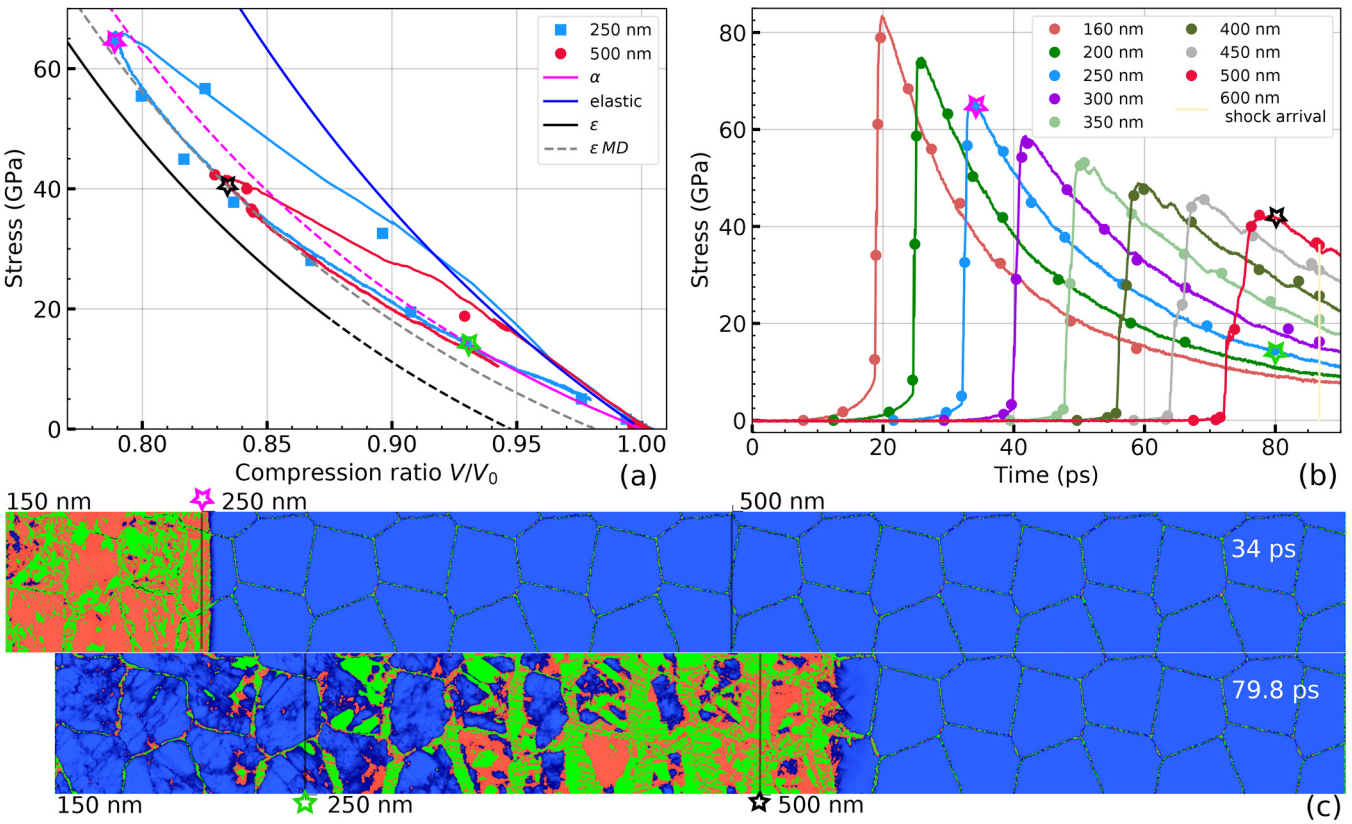

FIG. 7. (a) Stress–strain $\sigma - V/V_0$ pathways obtained directly from MD simulation (solid lines) and the points of the same color reconstructed with the inverse analysis for 250 and 500 nm films. (b) Directly obtained (solid lines) and reconstructed stress-time data (symbols) for several Lagrangian particles with different initial coordinates. (c) Shock propagation in polycrystalline iron initiates phase transition illustrated by 2D maps of local order parameters from MD simulation. Blue, red, and green show the α, γ, and ε iron phases, respectively. The asterisks indicate the positions of Lagrangian particles with the initial coordinates of 250 and 500 nm at times 34 and 79.8 ps, respectively. The left edge of the sample is driven by a piston with velocity from 2T hydrodynamic modeling, see details in Sec. III D.

to the orientation of the coordinate system and the rotation transformations of atom coordinates. Moreover, the order parameters with $l = 4$ and $l = 6$ distinguish well the type of crystal lattice at high temperatures.[65]

Position in a Q_4–Q_6 plane determines the coloring of the crystalline phases of iron in Fig. 7(c), including at temperatures such that the ranges of possible values of Q_4 and Q_6 for different types of crystal lattices can overlap. The *bcc*-phase is characterized by $Q_4^{bcc} = 0.036\,369\,65$ and $Q_6^{bcc} = 0.510\,688\,2$ for an ideal *bcc* lattice; a *hcp*-phase has $Q_4^{hcp} = 0.097\,222\,22$ and $Q_6^{hcp} = 0.484\,761\,7$; an *fcc* lattice has $Q_4^{fcc} = 0.190\,940\,7$ and $Q_6^{fcc} = 0.574\,524\,3$. The geometrical proximity of *fcc* and *hcp* lattices makes it difficult to distinguish them; moreover, the used EAM potential provides very similar enthalpy of formation of both phases at high pressures. However, the coexistence of both ε and γ of the iron phases was experimentally observed after short laser action.[66] To separate different lattices by local parameters of C_S, Q_4, *and*Q_6, a sequence of rules is applied. First, the central symmetry parameter is checked for the condition that the given substance is just a crystal; thus, the liquid phase is separated by the condition $C_S < 2.5$. Second, the cubic lattices are distinguished from the hexagonal *hcp* by the condition $C_S > 4.9$. Then for a pixel where $Q_4 > Q_4^{hcp}$, an *fcc* is assumed, and *bcc* in the opposite case.

Our MD simulation indicates that the phase states on a stress–strain diagram calculated by the inverse analysis correspond to the same states observed directly on MD-based 2D maps. As is obvious from the diagram and maps shown in Fig. 7(c), two informative slices (marked by magenta and green stars) representing the 250 nm Lagrangian particle at times of 34 and 79.8 ps consist of ε and α phases, which are both placed at the plastic shock Hugoniots of the correspondent phases in Fig. 7(a) as expected. The third slice (black star) with the 500 nm Lagrangian particle at 79.8 ps is also correctly placed on the plastic shock Hugoniot for ε-iron.

E. Inverse analysis technique results

Let us apply the above described and validated inverse analysis technique to our experimental data in order to reconstruct the stress–strain pathways on phase diagrams of iron. Figure 3 shows the selection of a set of reference points—10 at each profile times 5

profiles for different iron film thicknesses. As a result, the simplified profiles are obtained and shown in Fig. 3 by the dashed straight lines connecting the adjacent points. On each profile, the first point 1 refers to the arrival of the wave, the points 2-3-4-5-6 rising to the maximum amplitude were selected at some peculiarities (like a knee) of profiles. The points 7-8-9-10 correspond to the decreasing part of profile. Ten functions $u_i(h)$ and $t_i(h)$ for each set of 5 points define a function of two variables, which is shown in Fig. 4, where the dashed lines mark the piecewise linear functions $t_i(h)$.

Figure 8 shows the reconstructed stress–strain diagrams for films with thicknesses of 480, 580, 740, and 970 nm. Equations (4) and (5) are numerically integrated using the boundary condition of zero velocity before SW arrival $u(h, t_1(h)) = 0$. The lower limit of integration over the variables h or t for the data $t_1(h)$ or $h_1(t)$ corresponds to the points on the lower dashed curve in Fig. 4. In contrast to Ref. 47, there is no explicit account of discontinuities in the approximation of $u(h, t)$—all points are connected by a piecewise linear interpolation. Numerical integration of the functions (4) and (5) is performed using the Quadpack library.[67] The calculation procedure[68] was implemented by the interactive Python scripts and Jupyter notebooks.[69]

The inverse analysis technique is carried out in the interpolation region only. Therefore, we are limited by the arrival time of the elastic wave for a profile for greatest thickness h. The arrival time is marked with a solid line in Fig. 4. Thus, for calculating σ-V/V_0, the last moment of approximately 160 ps is achieved in interpretation of experiment with the 970 nm film. Figure 8 shows the phase diagram of the Lagrangian particles for films of 480, 580, 740, and 970 nm. The elastic shock Hugoniot is plotted using the points numbered 2 on the profiles from Fig. 3. For the first profile, the shock velocity U_s is estimated from the film width and arrival time, and for other films, the U_s is estimated from a ratio of the film thicknesses difference to the time difference for the points numbered 2 from the current and previous profiles with a smaller thickness. The shock Hugoniot parameter $c_a = 6$ km/s is assumed to be equal to the speed of sound from Ref. 20. The parameter $s_a = 1.148$ is calculated using the least squares method.

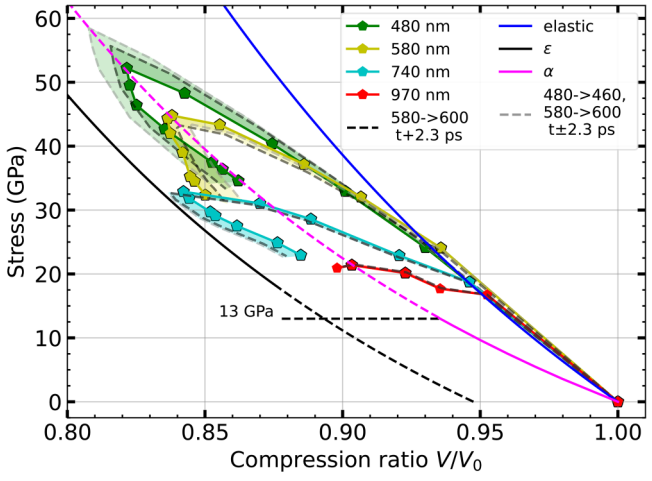

FIG. 8. Phase curve reconstruction via the inverse analysis of the kinematic data $u(h, t)$. The points correspond to the set of reference points from Fig. 3. The dashed lines show alternative stress–strain curves for varied arrival times and film thicknesses.

The plastic shock Hugoniots are based on experimental data[43] with the following set of parameters $c_a^\alpha = 4.63$ km/s, $s_a^\alpha = 1.33$, and $\rho_0^\alpha = 7.874\,\mathrm{kg/m^3}$ for the α-iron and $c_a^\varepsilon = 4.63$ km/s, $s_a^\varepsilon = 1.33$, and $\rho_0^\varepsilon = 8.31\,\mathrm{kg/m^3}$ for ε-iron. Pressure of 13 GPa marks the boundary of existence of a stable α-phase of iron at room temperature. The solid line in Fig. 8 shows the shock Hugoniot up to the lowest pressure in the experimental data for the ε-iron. The metastable phases are represented by dashed lines. Calculation results are investigated for the effect of varying the film thickness and the corresponding time of the SW arrival. Figure 8 shows two variation cases: the first option increases the thickness of the 580 nm film to 600 nm and the corresponding arrival time delay by 2.3 ps (black dotted line); second, in addition to varying the 580 nm film, the thickness of the 480 film was reduced to 460 nm, taking into account the earlier arrival of the wave by 2.3 ps (gray dotted line).

IV. DISCUSSION

We have found that an ultrashort laser-driven shock wave may initiate polymorphic $\alpha \rightarrow \varepsilon$ transformation in iron if the shock stress exceeds at least 20 GPa. The inference about phase transformation is based on the intersections of a Lagrangian particle pathway with the shock Hugoniot in the stress–strain diagram as shown in Fig. 8. It is seen that the polymorphic transformation proceeds in an unloading tail after the shock jump, and it may not be completed if the unloading time is too short. Using the inverse analysis technique, it is shown that the transformation is partial in the 480 and 580 films, and it is completed in the 740 nm film only.

The maximal stress at shock jump is observed in the 480 nm thick film of α-iron. This jump is followed by an unloading wave, in which the stress decreases but remains rather high $\gtrsim$30 GPa until the end of analysis. During unloading, the observed partial transformation to the ε-phase changes into a backward transition to the metastable α-phase at such high compression. This phenomenon is unusual since the experimental backward transition pressure is up to 10 GPa during unloading from 23[70] or 13 GPa in hydrostatic isothermal compression.[38] In order to check the accuracy of the inverse analysis method, we vary the arrival times and film thicknesses, but the analysis results remain qualitatively the same, as illustrated by dispersion of dashed stress–strain curves in Fig. 8.

A similar initial stress–strain pathway is observed in the film with a thickness of 580 nm—the maximum of pressure is reached at the α-phase plastic shock Hugoniot. But there is a partial transformation into the ε-phase which occurs in the unloading tail. The alternative results shown in Fig. 8 by dashed lines demonstrate that both further transformation into the ε-phase and a backward transition to the α-phase are possible. The $\alpha \rightarrow \varepsilon$ transition is assumed to be completed in the 740 nm thick film because the maximum stress reaches the ε-phase shock Hugoniot. The following

unloading results in a gradual transition back to the α-iron. In the film with thickness of 970 nm, the recorded velocity profile is too short since it is limited by the arrival of an elastic SW to the rear side of the 1160 nm film. This arrival time limits the range of stress interpolation in the h–t plane. Additional experimental results are needed to reconstruct the stress–strain pathway in the 970 nm film.

The shock-induced $\alpha \rightarrow \varepsilon$ transition at lower strain rates is also discussed in Ref. 21 with the help of a similar inverse analysis techniques, but it fully completes behind a shock front. We think that it happens because the unloading tail lasts several hundreds of picoseconds. In contrast to our work, the shock jumps are followed by the sharp unloading tails lasting tens of picoseconds, which may cease the phase transition until its stopping and initiate the backward $\varepsilon \rightarrow \alpha$ transition as it is observed in the 740 nm film and, surprisingly, in the 480 nm film regardless of the high stress there, see Fig. 8.

The qualitative behavior of the observed backward transition is reproduced in our combined 2T hydrodynamic and MD simulation illustrated in Fig. 7. Such a combined approach provides a straightforward way to study the transition rates in distinct grains of polycrystalline iron under the compression and unloading waves. The width of unloading tail where ε-phase coexists with γ-phase is approximately 150 nm. The transition width is determined by a time during which the unloading stress remains above approximately 20 GPa, which lasts tens of picoseconds. Lower stress leads to backward transition to the α-phase. MD simulation of polycrystalline iron exhibits arrest of polymorphic transformation at the grain boundaries. It results in the coexistence of different iron phases in neighbor grains with different lattice orientations.

ACKNOWLEDGMENTS

The authors would like to thank K. V. Khishchenko for the equation of states and Yu. V. Petrov for electron subsystem formulae for 2T hydrodynamics modeling. This research was supported by The Ministry of Science and Higher Education of the Russian Federation (Agreement with Joint Institute for High Temperatures RAS No 075-15-2020-785 dated September 23, 2020).

AUTHOR DECLARATIONS

Conflict of Interest

The authors have no conflicts to disclose.

DATA AVAILABILITY

The data that support the findings of this study are available within article and from the corresponding author upon reasonable request. Inverse analysis calculation procedures producing the article figures are openly available in Zenodo repository, Ref. 69.

REFERENCES

[1]S. I. Anisimov, A. M. Prokhorov, and V. E. Fortov, "Application of high-power lasers to study matter at ultrahigh pressures," Sov. Phys. Usp. **27**, 181 (1984).
[2]G. I. Kanel', V. E. Fortov, and S. V. Razorenov, "Shock waves in condensed-state physics," Phys. Usp. **50**, 771 (2007).
[3]R. Evans, A. D. Badger, F. Fallies, M. Mahdieh, T. A. Hall, P. Audebert, J.-P. Geindre, J.-C. Gauthier, A. Mysyrowicz, G. Grillon, and A. Antonetti, "Time- and space-resolved optical probing of femtosecond-laser-driven shock waves in aluminum," Phys. Rev. Lett. **77**, 3359–3362 (1996).
[4]K. T. Gahagan, D. S. Moore, D. J. Funk, R. L. Rabie, S. J. Buelow, and J. W. Nicholson, "Measurement of shock wave rise times in metal thin films," Phys. Rev. Lett. **85**, 3205 (2000).
[5]D. J. Funk, D. S. Moore, K. T. Gahagan, S. J. Buelow, J. H. Reho, G. L. Fisher, and R. L. Rabie, "Ultrafast measurement of the optical properties of aluminum during shock-wave breakout," Phys. Rev. B **64**, 115114 (2001).
[6]K. T. Gahagan, D. S. Moore, D. J. Funk, J. H. Reho, and R. L. Rabie, "Ultrafast interferometric microscopy for laser-driven shock wave characterization," J. Appl. Phys. **92**, 3679 (2002).
[7]V. V. Zhakhovskii and N. A. Inogamov, JETP Lett. **92**, 521 (2010).
[8]V. V. Zhakhovsky, M. M. Budzevich, N. A. Inogamov, I. I. Oleynik, and C. T. White, "Two-zone elastic-plastic single shock waves in solids," Phys. Rev. Lett. **107**, 135502 (2011).
[9]N. A. Inogamov, V. V. Zhakhovskii, V. A. Khokhlov, and V. V. Shepelev, "Superelasticity and the propagation of shock waves in crystals," JETP Lett. **93**, 226–232 (2011).
[10]S. I. Ashitkov, M. Agranat, G. I. Kanel', P. S. Komarov, and V. Fortov, "Behavior of aluminum near an ultimate theoretical strength in experiments with femtosecond laser pulses," JETP Lett. **92**, 516 (2010).
[11]V. H. Whitley, S. D. McGrane, D. E. Eakins, C. A. Bolme, D. S. Moore, and J. F. Bingert, "The elastic-plastic response of aluminum films to ultrafast laser-generated shocks," J. Appl. Phys. **109**, 013505 (2011).
[12]J. C. Crowhurst, M. R. Armstrong, K. B. Knight, J. M. Zaug, and E. M. Behymer, "Invariance of the dissipative action at ultrahigh strain rates above the strong shock threshold," Phys. Rev. Lett. **107**, 144302 (2011).
[13]R. F. Smith, J. H. Eggert, R. E. Rudd, D. C. Swift, C. A. Bolme, and G. Collins, "High strain-rate plastic flow in Al and Fe," J. Appl. Phys. **110**, 123515 (2011).
[14]G. I. Kanel, "Rate and temperature effects on the flow stress and tensile strength of metals," AIP Conf. Proc. **1426**, 939 (2012).
[15]V. V. Zhakhovsky, N. A. Inogamov, B. J. Demaske, I. I. Oleynik, and C. T. White, "Elastic-plastic collapse of super-elastic shock waves in face-centered-cubic solids," J. Phys.: Conf. Ser. **500**(17), 172007 (2014).
[16]B. J. Demaske, V. V. Zhakhovsky, N. A. Inogamov, and I. I. Oleynik, "Ultrashort shock waves in nickel induced by femtosecond laser pulses," Phys. Rev. B **87**, 054109 (2013).
[17]R. Perriot, V. V. Zhakhovsky, N. A. Inogamov, and I. I. Oleynik, "Evolution of elastic precursor and plastic shock wave in copper via molecular dynamics simulations," J. Phys.: Conf. Ser. **500**, 172008 (2014).
[18]K. Khishchenko and A. Mayer, "High- and low-entropy layers in solids behind shock and ramp compression waves," Int. J. Mech. Sci. **189**, 105971 (2020).
[19]S. I. Ashitkov, M. B. Agranat, G. I. Kanel, and V. E. Fortov, "Approaching the ultimate shear and tensile strength of aluminum in experiments with femtosecond pulse laser," AIP Conf. Proc. **1426**, 1081 (2012).
[20]S. I. Ashitkov, P. S. Komarov, M. B. Agranat, G. I. Kanel, and V. E. Fortov, "Achievement of ultimate values of the bulk and shear strengths of iron irradiated by femtosecond laser pulses," JETP Lett. **98**, 384 (2013).
[21]J. C. Crowhurst, B. W. Reed, M. R. Armstrong, H. B. Radousky, J. A. Carter, D. C. Swift, J. M. Zaug, R. W. Minich, N. E. Teslich, and M. Kumar, "The $\alpha \rightarrow \epsilon$ phase transition in iron at strain rates up to $\sim 10^9$ s^{-1}," J. Appl. Phys. **115**, 113506 (2014).
[22]S. I. Ashitkov, P. S. Komarov, E. V. Struleva, M. B. Agranat, and G. I. Kanel, "Mechanical and optical properties of vanadium under shock picosecond loads," JETP Lett. **101**, 276 (2015).
[23]N. A. Inogamov, V. V. Zhakhovskii, S. I. Ashitkov, Y. V. Petrov, M. B. Agranat, S. I. Anisimov, K. Nishihara, and V. E. Fortov, "Nanospallation induced by an ultrashort laser pulse," J. Exp. Theor. Phys. **107**, 1 (2008).
[24]N. A. Inogamov, V. A. Khokhlov, Y. V. Petrov, and V. V. Zhakhovsky, "Hydrodynamic and molecular-dynamics modeling of laser ablation in liquid: From surface melting till bubble formation," Opt. Quant. Electron. **52**, 63 (2020).

[25]N. A. Inogamov, Y. V. Petrov, S. I. Anisimov, A. M. Oparin, N. V. Shaposhnikov, D. von der Linde, and J. Meyer-ter Vehn, "Expansion of matter heated by an ultrashort laser pulse," JETP Lett. **69**, 310 (1999).
[26]S. I. Anisimov, V. V. Zhakhovskii, N. A. Inogamov, K. Nishihara, A. M. Oparin, and Y. V. Petrov, "Destruction of a solid film under the action of ultrashort laser pulse," JETP Lett. **77**, 606 (2003).
[27]R. Fabbro, J. Fournier, P. Ballard, D. Devaux, and J. Virmont, "Physical study of laser-produced plasma in confined geometry," J. Appl. Phys. **68**, 775 (1990).
[28]N. A. Inogamov, V. V. Khokhlov, and V. A. Zhakhovsky, "Formation of a single microstructure and ablation into a transparent insulator under subnanosecond laser irradiation," JETP Lett. **108**, 439–445 (2018).
[29]Y. V. Petrov, N. A. Inogamov, V. V. Zhakhovsky, and V. A. Khokhlov, "Condensation of laser produced gold plasma during expansion and cooling in water environment," Contrib. Plasma Phys. **59**, e201800180 (2019).
[30]G. I. Kanel, E. B. Zaretsky, S. V. Razorenov, S. I. Ashitkov, and V. E. Fortov, "Unusual plasticity and strength of metals at ultra-short load durations," Phys. Usp. **60**, 490 (2017).
[31]G. I. Kanel, S. V. Razoreno, G. V. Garkushin, S. I. Ashitkov, P. S. Komarov, and M. B. Agranat, "Deformation resistance and fracture of iron over a wide strain rate range," Phys. Solid State **56**, 1569 (2014).
[32]J. P. Geindre, P. Audebert, S. Rebibo, and J. C. Gauthier, "Single-shot spectral interferometry with chirped pulses," Opt. Lett. **26**, 1612 (2001).
[33]S. Ogata, J. Li, N. Hirosaki, Y. Shibutani, and S. Yip, "Ideal shear strain of metals and ceramics," Phys. Rev. B **70**, 104104 (2004).
[34]D. Clatterbuck, D. Chrzan, and J. Morris, "The ideal strength of iron in tension and shear," Acta Mater. **51**, 2271 (2003).
[35]L. V. Al'tshuler, "Use of shock waves in high-pressure physics," Phys. Usp. **8**, 52 (1965).
[36]G. I. Kerley, "Multiphase equation of state for iron," Report No. SAND93-0027 (Sandia National Laboratories, Albuquerque, NM, 1993).
[37]D. Bancroft, E. L. Peterson, and M. S, "Polymorphism of iron at high pressure," J. Appl. Phys. **27**, 291–298 (1956).
[38]L. M. Barker and R. E. Hollenbach, "Shock wave study of the $\alpha \rightarrow \varepsilon$ phase transition in iron," J. Appl. Phys. **45**, 4872 (1974).
[39]G. E. Duvall and R. A. Graham, "Phase transitions under shock-wave loading," Rev. Mod. Phys. **49**, 523 (1977).
[40]A. V. Ananyin, A. N. Dremin, and G. I. Kanel', "Polymorphic transformation of iron in a shock wave," Phys. Combust. Explosion **3**, 93 (1981).
[41]V. D. Gluzman, G. I. Kanel', V. F. Loskutov, V. E. Fortov, and E. I. Horev, "Resistance to deformation and destruction of steel 35khznm under shock loading," Prob. Strength **8**, 52 (1985).
[42]S. A. Dyachkov, D. K. Ilnitsky, A. N. Parshikov, and V. V. Zhakhovsky, "The model of iron properties for plate impact and explosive compression simulations," J. Phys.: Conf. Ser. **1556**, 012032 (2020).
[43]S. I. Ashitkov, V. V. Zhakhovsky, N. A. Inogamov, P. S. Komarov, M. B. Agranat, and G. I. Kanel, "The behavior of iron under ultrafast shock loading driven by a femtosecond laser," AIP Conf. proc. **1793**, 100035 (2017).
[44]V. Zhakhovsky, K. Migdal, N. Inogamov, and S. Anisimov, "MD simulation of steady shock-wave fronts with phase transition in single-crystal iron," AIP Conf. Proc. **1793**, 070003 (2017).
[45]J. B. Aidun and Y. M. Gupta, "Analysis of Lagrangian gauge measurements of simple and nonsimple plane waves," J. Appl. Phys. **69**, 6998 (1991).
[46]J. C. Boettger and D. C. Wallace, "Metastability and dynamics of the shock-induced phase transition in iron," Phys. Rev. B **55**, 2840 (1997).
[47]B. W. Reed, J. S. Stolken, R. W. Minich, and M. Kumar, "A unified approach for extracting strength information from nonsimple compression waves. part i: Thermodynamics and numerical implementation," J. Appl. Phys. **110**, 113505 (2011).
[48]B. W. Reed, J. Reed Patterson, D. C. Swift, J. S. Stolken, R. W. Minich, and M. Kumar, "A unified approach for extracting strength information from non-simple compression waves. part ii. Experiment and comparison with simulation," J. Appl. Phys. **110**, 113506 (2011).
[49]T. Q. Qiu and C. L. Tien, "Heat transfer mechanisms during short-pulse laser heating of metals," J. Heat Transf. **115**(4), 835–841 (1993).
[50]V. V. Temnov, K. Sokolowski-Tinten, P. Zhou, and D. von der Linde, "Ultrafast imaging interferometry at femtosecond-laser-excited surfaces," J. Opt. Soc. Am. B **23**, 1954 (2006).
[51]G. I. Kanel, V. E. Fortov, and S. V. Razorenov, "Polymorphic transformations and phase transitions in shock-compressed solids," in *Shock-Wave Phenomena and the Properties of Condensed Matter* (Springer New York, New York, 2004), pp. 189–216.
[52]N. A. Inogamov, V. V. Zhakhovskii, and V. A. Khokhlov, "Dynamics of gold ablation into water," J. Exp. Theor. Phys. **127**(1), 79 (2018).
[53]S. I. Anisimov, B. L. Kapeliovich, and T. L. Perel'man, "Electron emission from metal surfaces exposed to ultrashort laser pulses," Sov. Phys. JETP **39**, 375 (1974).
[54]S. I. Anisimov, V. V. Zhakhovskii, N. A. Inogamov, K. Nishihara, Y. V. Petrov, and V. A. Khokhlov, "Ablated matter expansion and crater formation under the action of ultrashort laser pulse," J. Experim. Theor. Phys. (JETP) **103**, 183 (2006).
[55]N. A. Inogamov, S. I. Anisimov, Y. V. Petrov, V. A. Khokhlov, V. V. Zhakhovskii, K. Nishihara, M. B. Agranat, S. I. Ashitkov, and P. S. Komarov, "Theoretical and experimental study of hydrodynamics of metal target irradiated by ultrashort laser pulse," Proc. SPIE **7005**, 70052F (2008).
[56]K. V. Khishchenko, "Equations of state for two alkali metals at high temperatures," J. Phys.: Conf. Ser. **98**, 032023 (2008).
[57]K. V. Khishchenko, "Equation of state for tungsten over a wide range of densities and internal energies," J. Phys.: Conf. Ser. **653**, 012081 (2015).
[58]K. V. Khichshenko, "Equation of state of sodium for modeling of shock-wave processes at high pressures," Math. Montis. **40**, 140 (2017).
[59]V. A. Khokhlov, Y. V. Petrov, N. A. Inogamov, K. P. Migdal, J. Winter, C. Aichele, S. Rapp, and H. P. Huber, "Dynamics of supported ultrathin molybdenum films driven by strong short laser impact," J. Phys.: Conf. Ser. **1147**, 012066 (2019).
[60]V. A. Khokhlov, S. I. Ashitkov, N. A. Inogamov, P. S. Komarov, A. N. Parshikov, Y. V. Petrov, S. A. Romashevsky, E. V. Struleva, P. A. Tsygankov, and V. V. Zhakhovsky, "Laser ablation of a multilayer target with layers of nanometer thickness," J. Phys.: Conf. Ser. **1787**, 012022 (2021).
[61]Y. Petrov, K. Migdal, N. Inogamov, V. Khokhlov, D. Ilnitsky, I. Milov, N. Medvedev, V. Lipp, and V. Zhakhovsky, "Ruthenium under ultrafast laser excitation: Model and dataset for equation of state, conductivity, and electron-ion coupling," Data Brief **28**, 104980 (2020).
[62]P. J. Steinhardt, D. R. Nelson, and M. Ronchetti, "Bond-orientational order in liquids and glasses," Phys. Rev. B **28**, 784 (1983).
[63]W. Lechner and C. Dellago, "Accurate determination of crystal structures based on averaged local bond order parameters," J. Chem. Phys. **129**, 114707 (2008).
[64]C. L. Kelchner, S. J. Plimpton, and J. C. Hamilton, "Dislocation nucleation and defect structure during surface indentation," Phys. Rev. B **58**, 11085 (1998).
[65]B. A. Klumov, S. A. Khrapak, and G. E. Morfill, "Structural properties of dense hard sphere packings," Phys. Rev. B **83**, 184105 (2011).
[66]H. Hwang, E. Galtier, H. Cynn, I. Eom, S. H. Chun, Y. Bang, G. C. Hwang, J. Choi, T. Kim, M. Kong, S. Kwon, K. Kang, H. J. Lee, C. Park, J. I. Lee, Y. Lee, W. Yang, S.-H. Shim, T. Vogt, S. Kim, J. Park, S. Kim, D. Nam, J. H. Lee, H. Hyun, M. Kim, T.-Y. Koo, C.-C. Kao, T. Sekine, and Y. Lee, "Subnanosecond phase transition dynamics in laser-shocked iron," Sci. Adv. **6**, aaz5132 (2020).
[67]R. Piessens, E. De Doncker-Kapenga, E. de C. Ueberhuber, and D. Kahaner, *Quadpack: A Subroutine Package for Automatic Integration*, Computational Mathematics Series (Springer-Verlag, 1983).
[68]S. A. Murzov, *The Inverse Analysis Procedures* (Zenodo, 2021).
[69]T. Kluyver, B. Ragan-Kelley, F. Pérez, B. Granger, M. Bussonnier, J. Frederic, K. Kelley, J. Hamrick, J. Grout, S. Corlay, P. Ivanov, D. Avila, S. Abdalla, C. Willing, and J. development team, "Jupyter notebooks—A publishing format for reproducible computational workflows," in *Positioning and Power in Academic Publishing: Players, Agents and Agendas*, edited by F. Loizides and B. Scmidt (IOS Press, 2016), pp. 87–90.
[70]T. J. Ahrens, "Shock wave experiments," in *Encyclopedia of Geomagnetism and Paleomagnetism*, edited by D. Gubbins and E. Herrero-Bervera (Springer Netherlands, Dordrecht, 2007), pp. 912–920.